The Astronomical Journal, 171:287 (11pp), 2026 May https://doi.org/10.3847/1538-3881/ae5484

Antisolar Differential Rotation May Have Revived Magnetic Braking in the Subgiant 31 Aquilae

Travis S. Metcalfe[1], Jennifer L. van Saders[2], Thomas R. Ayres[3], Derek Buzasi[4], Jeremy J. Drake[5], Ricky Egeland[1], Rafael A. García[6], Oleg Kochukhov[7], Steven H. Saar[8], Keivan G. Stassun[9], Sarbani Basu[10], J. M. Joel Ong[11], Amalie Stokholm[12], Timothy R. Bedding[11], Sylvain N. Breton[13], Ilya V. Ilyin[14], Pascal Petit[15], Marc H. Pinsonneault[16], and Klaus G. Strassmeier[14]

[1] Center for Solar–Stellar Connections, WDRC, 9020 Brumm Trail, Golden, CO 80403, USA
[2] Institute for Astronomy, University of Hawai'i, 2680 Woodlawn Drive, Honolulu, HI 96822, USA
[3] Center for Astrophysics and Space Astronomy, 389 UCB, University of Colorado, Boulder, CO 80309, USA
[4] Department of Astronomy & Astrophysics, University of Chicago, 5640 S. Ellis Avenue, Chicago, IL 60637, USA
[5] Lockheed Martin Solar and Astrophysics Laboratory, 3251 Hanover Street, Palo Alto, CA 94304, USA
[6] Université Paris-Saclay, Université Paris Cité, CEA, CNRS, AIM, 91191, Gif-sur-Yvette, France
[7] Department of Physics and Astronomy, Uppsala University, Box 516, SE-75120 Uppsala, Sweden
[8] Harvard-Smithsonian Center for Astrophysics, Cambridge, MA 02138, USA
[9] Department of Physics & Astronomy, Vanderbilt University, 6301 Stevenson Center Lane, Nashville, TN 37235, USA
[10] Department of Astronomy, Yale University, PO Box 208101, New Haven, CT 06520-8101, USA
[11] Sydney Institute for Astronomy (SIfA), School of Physics, University of Sydney, Camperdown, NSW 2006, Australia
[12] School of Physics & Astronomy, University of Birmingham, Edgbaston, Birmingham, B15 2TT, UK
[13] INAF—Osservatorio Astrofisico di Catania, Via S. Sofia, 78, 95123 Catania, Italy
[14] Leibniz-Institut für Astrophysik Potsdam (AIP), An der Sternwarte 16, D-14482 Potsdam, Germany
[15] Université de Toulouse, CNRS, CNES, 14 Avenue Edouard Belin, 31400, Toulouse, France
[16] Department of Astronomy, The Ohio State University, 140 West 18th Avenue, Columbus, OH 43210, USA

Received 2026 February 11; revised 2026 March 15; accepted 2026 March 17; published 2026 April 14

Abstract

Recent observations have shown that sufficiently slow rotation disrupts the organization of large-scale magnetic field in older main-sequence stars, leading to weakened magnetic braking (WMB) and a collapse in the efficiency of the global stellar dynamo. Recent simulations predict a shift from solar-like to antisolar differential rotation (DR) at slower rotation rates, which typically do not occur on the main sequence due to WMB. However, physical expansion on the subgiant branch can eventually slow the stellar rotation beyond this threshold, yielding a noncycling large-scale field that revives magnetic braking. We combine asteroseismology from the Transiting Exoplanet Survey Satellite (TESS) with spectropolarimetry from the Large Binocular Telescope (LBT) to test these predictions in the old metal-rich subgiant 31 Aql. The LBT observations reveal a strong large-scale magnetic field in this star, and archival measurements of its chromospheric emission over 50 yr confirm that it is noncycling, as predicted. The star exhibits a variety of rotation periods during different observing seasons, consistent with DR but with no means of distinguishing between solar-like and antisolar patterns. We incorporate the TESS observations to estimate the current wind-braking torque of 31 Aql, demonstrating that it supports revived magnetic braking in this old subgiant. We also use rotational evolution modeling to place a preliminary constraint on the stellar Rossby number for the transition to antisolar DR. Future refinements in both asteroseismic observations and rotational modeling may yield improvements to this initial analysis.

Unified Astronomy Thesaurus concepts: Spectropolarimetry (1973); Stellar activity (1580); Stellar evolution (1599); Stellar oscillations (1617); Stellar rotation (1629)

1. Introduction

The influence of stellar rotation on global convective patterns changes dramatically throughout the lives of solar-type stars. In the earliest phases of stellar evolution, rapid rotation is thought to imprint a cylindrical pattern of differential rotation (DR) on the outer convection zone, with a fast equator and slower poles in a configuration known as the Taylor–Proudman state (J. Proudman 1916; G. I. Taylor 1917). As the magnetized stellar wind gradually sheds angular momentum, rotation slows and the DR pattern is thought to become more conical, as observed in the Sun (M. J. Thompson et al. 1996), with contours of constant rotation extending almost radially through the convection zone rather than parallel to the rotation axis. When the rotation rate becomes comparable to the convective overturn timescale (τ_c), a broad array of convection simulations suggest that the DR pattern will flip from solar-like to antisolar, with a slow equator and faster poles (T. Gastine et al. 2014). However, observational confirmation of antisolar DR has been mostly confined to red giant stars (M. Weber et al. 2005).

Our understanding of stellar rotational evolution has been updated substantially over the past decade, modifying our expectations for the detection of antisolar DR. After stars contract onto the main sequence and magnetic braking begins to dominate their rotational evolution, the empirical relations of A. Skumanich (1972) approximate the decline of stellar activity and the gradual slowing of rotation with the square root of stellar age. The discovery of weakened magnetic braking (WMB; J. L. van Saders et al. 2016) in old Kepler field

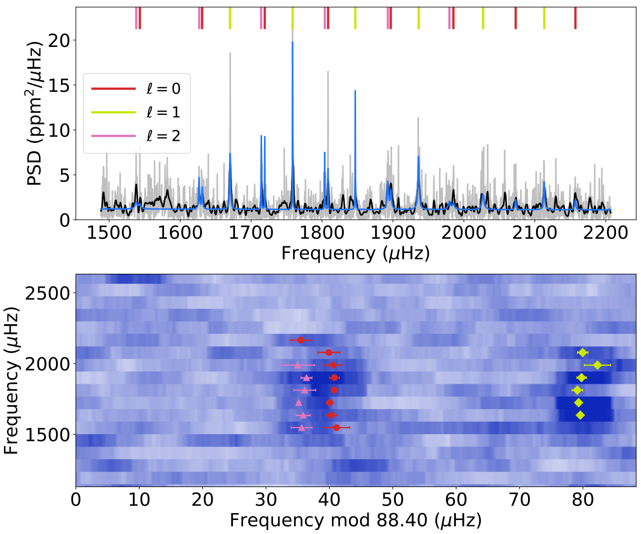

Figure 1. Top: power spectral density (PSD) in the frequency range of the fitted modes. In gray is the raw spectrum and in black a smoothed PSD. The blue line represents the fitted spectrum. The vertical red, yellow, and magenta bars indicate the central frequencies of the $\ell = 0$, 1, and 2 modes, respectively. Bottom: échelle diagram with $\Delta\nu = 88.40\mu$Hz. The fitted modes and their associated uncertainties are shown as circles, diamonds, and triangles with the same color-coding as in the top panel.

stars was the first indication that this orderly progression does not continue indefinitely, but is disrupted at activity levels close to solar (T. S. Metcalfe et al. 2016). Observational constraints on the large-scale magnetic field strength and the mass-loss rates of older stars revealed unexpected changes in both properties that combine to produce WMB and keep stellar rotation nearly constant during the second half of main-sequence lifetimes (T. S. Metcalfe et al. 2025). Consequently, stars may not reach the slow rotation rates that are required for the shift to antisolar DR until the physical expansion associated with core hydrogen exhaustion finally pushes them over this threshold.

Recent simulations predict observational signatures accompanying the shift from solar-like to antisolar DR, including the emergence of a noncycling large-scale magnetic field. Dynamo simulations described by A. S. Brun et al. (2022, see their Figure 13) appear to show a gradual transition from short activity cycles in rapidly rotating models to longer Sun-like cycles at intermediate rotation near the solar rate, and no cycles for models rotating more slowly than the Sun. Similar results were reported by A. Strugarek et al. (2017) for a completely independent set of dynamo simulations, and both sets of models lend qualitative support to the evolutionary scenario proposed by T. S. Metcalfe & J. van Saders (2017). The simulations also appear to show a gradual decline in the large-scale magnetic field strength as activity cycles grow longer, reaching a minimum near the solar rotation rate and increasing once again for more slowly rotating models with no cycles and antisolar DR (Q. Noraz et al. 2024; see also B. B. Karak et al. 2015; A. Brandenburg & M. S. Giampapa 2018). These results suggest that stars with antisolar DR might be expected to show "flat activity" from a stationary large-scale magnetic field. Crucially, the rotation rates required to produce antisolar DR in the simulations appear slower than FGK stars can typically reach on the main sequence under the influence of WMB.

The metal-rich G7 subgiant 31 Aql (b Aql, HD 182572, TIC 359981217) may have already evolved through the transition to antisolar DR. In more than 50 yr of chromospheric activity monitoring from the Mount Wilson survey (S. L. Baliunas et al. 1995) and the Keck Observatory (A. C. Baum et al. 2022), 31 Aql shows minimal long-term variability around a low average activity level ($\log R'_{\rm HK} = -5.1$), while the short-term variability is sufficient to measure a rotation period of $P_{\rm rot} \sim 41$ days (S. Baliunas et al. 1996). The latter suggests a Rossby number (Ro $\equiv P_{\rm rot}/\tau_c$) that may be well above the solar value, potentially in the realm of antisolar DR. In Section 2, we analyze new and archival observations to characterize 31 Aql, including time-series photometry from the Transiting Exoplanet Survey Satellite (TESS; G. R. Ricker et al. 2014), spectropolarimetry from the Large Binocular Telescope (LBT), X-ray measurements from Chandra, and UV observations from Hubble. In Section 3, we use these observations to determine precise stellar properties from asteroseismology, and to constrain the evolutionary pathway that led to the current magnetic and rotational configuration. Finally, in Section 4, we discuss our results and compare them to the predictions of dynamo simulations, to assess the possibility that 31 Aql might exhibit antisolar DR.

2. Observations

Below we analyze new and archival observations of 31 Aql to characterize the stellar properties relevant to its magnetic and rotational evolution. In Section 2.1, we identify solar-like oscillation frequencies from recent TESS photometry. In Section 2.2, we analyze new LBT spectropolarimetry to estimate the large-scale magnetic field strength, and verify its persistence in archival observations. In Section 2.3, we use recent X-ray measurements from Chandra to estimate the mass-loss rate, and in Section 2.4 we present new UV observations from Hubble. In Section 2.5, we use archival Mount Wilson data to confirm the absence of an obvious activity cycle and to extract seasonal rotation measurements. Finally, in Section 2.6, we determine the bolometric luminosity from the spectral energy distribution (SED).

2.1. TESS Photometry

TESS observed 31 Aql at 120 s cadence during Sector 54 (see M. N. Lund et al. 2025) and at 20 s cadence during Sector 81 (2024 July 15—2024 August 10). In this analysis, we use only the Sector 81 data because the 20 s cadence has lower noise than 120 s cadence data for bright stars (D. Huber et al. 2022). We extracted the data from the raw image frames following the process described in M. B. Nielsen et al. (2020) and T. S. Metcalfe et al. (2023b), which uses aperture masks optimized to produce the highest signal-to-noise ratio (S/N) possible with simple aperture photometry on an isolated star; in this case, our mask contained 85 pixels from the 297 pixel postage stamp. Conservatively, we discarded observations with flag values greater than unity, leaving 106,244 data points with a duty cycle above 92%. Finally, we detrended the light curve against centroid pixel coordinates, breaking the time series into two parts separated by the data downlink gap starting near day 3519. The resulting light curve has a noise level that is approximately 11% lower compared to the Science Processing Operations Center (J. M. Jenkins et al. 2016) PDCSAP product. Prior to frequency analysis, the light curve

Table 1
Identified Oscillation Frequencies for 31 Aql

n	ℓ	ν (μHz)	σ_ν (μHz)
17	0	1543.92	2.09
18	0	1631.51	0.91
19	0	1719.66	0.57
20	0	1808.74	0.20
21	0	1897.20	0.81
22	0	1985.40	1.39
23	0	2073.11	1.75
24	0[a]	2157.08	1.71
18	1	1670.78	0.38
19	1	1758.92	0.17
20	1	1847.10	0.83
21	1	1936.18	0.75
22	1	2027.08	2.08
23	1	2113.15	0.83
16	2	1538.43	1.65
17	2	1627.07	1.16
18	2	1714.77	0.28
19	2	1804.10	1.74
20	2	1892.79	0.87
21	2	1979.80	2.67

Note.
[a] Possible misidentification of an ($n = 23$, $\ell = 2$) mode.

was gap-filled using a multiscale discrete cosine transform following inpainting principles (R. A. García et al. 2014; S. Pires et al. 2015), and high-pass filtered with a cutoff frequency of 100 μHz to minimize residual contributions from spacecraft jitter. The power spectrum of this light curve is illustrated in the top panel of Figure 1, with an échelle diagram in the bottom panel to facilitate the identification of the spherical harmonic degree (ℓ) for each frequency.

The solar-like oscillation frequencies were identified using the `apollinaire`[17] code (S. N. Breton et al. 2022), which is built upon the `emcee` ensemble Markov Chain Monte Carlo sampler (D. Foreman-Mackey et al. 2013). In this framework, each mode is described by a Lorentzian function, where both the central frequency and the line width are treated as independent parameters. Rather than fitting an individual height for each mode, a single height parameter is assigned "by order n", i.e., to all modes with $\ell = 0$, 1 at a given radial order n, and to $\ell = 2$ modes at order $n - 1$. The ratios of mode heights between different angular degrees are incorporated as global parameters. The free parameters for all modes were fit simultaneously in a global procedure, following the methodology pioneered by T. Roca Cortés et al. (1999) and improved by S. T. Fletcher et al. (2008), which helps to account for correlations between modes and provides a more robust estimation of the oscillation parameters (see also G. R. Davies et al. 2016; M. N. Lund et al. 2017). The identified oscillation frequencies and their uncertainties are listed in Table 1 and shown in Figure 1. Posterior probability distributions were generated for each parameter, and the median of each distribution was adopted as the central value. The adopted uncertainties are the average of the differences between the median and the 16th and 84th percentiles of the posterior distributions.

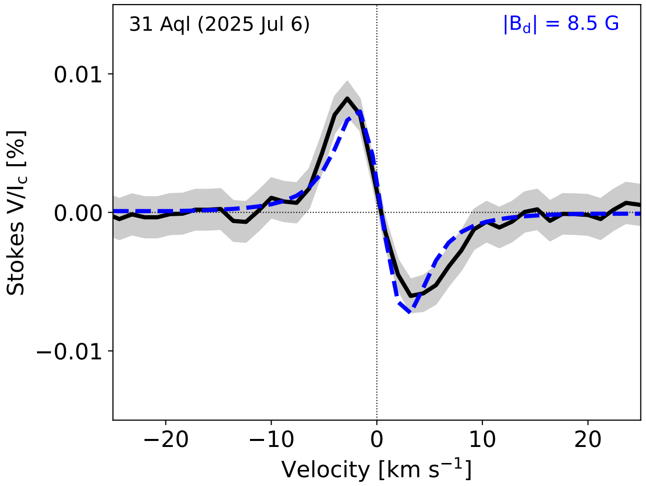

Figure 2. Stokes V polarization profile for 31 Aql from LBT observations on 2025 July 6. The observed LSD profile is shown as a black line, with uncertainties indicated by the gray shaded area. The dashed blue line is a model profile assuming an axisymmetric dipole morphology with a fixed inclination.

2.2. Spectropolarimetry

We observed 31 Aql with the Potsdam Echelle Polarimetric and Spectroscopic Instrument (PEPSI; K. G. Strassmeier et al. 2015) installed at the 2 × 8.4 m LBT. The observation comprised a single snapshot taken on 2025 July 6. We employed the same instrumental setup (spectral resolution $R = 130{,}000$, with wavelength coverage spanning the 475–540 and 623–743 nm regions) and data-reduction procedures as described in T. S. Metcalfe et al. (2019). Given the low expected amplitude of the polarization signal, we applied the least-squares deconvolution (LSD; J. F. Donati et al. 1997; O. Kochukhov et al. 2010) technique to extract high-S/N mean intensity and circular polarization profiles.

The line mask required for LSD was obtained from the Vienna Atomic Line Database (T. Ryabchikova et al. 2015), with atmospheric parameters $T_{\rm eff} = 5500$ K, $\log g = 4.0$, and metallicity $[{\rm M/H}] = +0.3$, comparable to J. M. Brewer et al. (2016). For the analysis of the PEPSI observation, we used 2568 metal lines deeper than 10% of the continuum. The LSD procedure yielded a polarization profile with a precision of 4.18 ppm and a clear detection of the stellar magnetic field, as illustrated in Figure 2. The Stokes V signature of 31 Aql corresponds to a mean longitudinal magnetic field $\langle B_z \rangle = 1.525 \pm 0.053$ G. For consistency with our previous analyses of Stokes V profiles, we estimated the strength of an axisymmetric dipole magnetic field using the modeling procedure described in T. S. Metcalfe et al. (2019), fixing the inclination angle at $i = 61^\circ$ (B. P. Bowler et al. 2023). This analysis yielded a dipole field strength of $B_{\rm d} = 8.5 \pm 1.1$ G. Due to geometric cancellation effects, adoption of an axisymmetric quadrupole or octupole yields a very strong magnetic field: $B_{\rm q} = 133 \pm 13$ G or $B_{\rm o} = 256 \pm 74$ G.

We complemented the PEPSI observation of 31 Aql with an analysis of archival spectropolarimetric data retrieved from PolarBase (P. Petit et al. 2014). This database includes two ESPaDOnS observations of 31 Aql obtained in 2007, as well as 15 NARVAL Stokes V spectra acquired over three nights in 2019. Both spectropolarimeters cover the 370–1000 nm wavelength range at a spectral resolution of $R = 65{,}000$. All spectra were processed using the same LSD procedure

---

[17] Documentation is available at https://apollinaire.readthedocs.io/.

described above, but employing a line mask consisting of 5306 spectral lines deeper than 20% of the continuum.

Among the 15 NARVAL observations, a definite Zeeman signature indicative of a global magnetic field was detected in every spectrum, whereas the two earlier ESPaDOnS observations yielded no detection owing to their lower S/N ratios. The LSD Stokes V profiles of 31 Aql obtained from NARVAL observations exhibit amplitudes of order $\sim 10^{-4}$ of the continuum, similar to the LSD profile derived from the PEPSI spectrum, enabling measurements of the mean longitudinal magnetic field in the range of 1–2 G with typical uncertainties of 0.3 G. The circular polarization signal appears stable, with no significant variability detected between nights. To further quantify the strength of the large-scale magnetic field in these archival spectra of 31 Aql, we selected the five NARVAL observations with the highest S/N ratios and applied the axisymmetric dipole fitting methodology described above. This analysis yielded an average dipole field strength of $B_{\rm d} = 7.9 \pm 0.7$ G, where the quoted uncertainty corresponds to the standard deviation of the fitting results for the individual spectra. Thus, the NARVAL measurements were consistent with those from PEPSI, suggesting long-term stability of the large-scale magnetic field.

2.3. X-Ray Measurements

The subgiant 31 Aql was captured in the ROSAT All-Sky survey in 1990 October as a faint source in 0.50 ks of accumulated exposure. The count rate was 0.029 ± 0.009 counts s^{-1} (0.1–2.4 keV) as reported in the rassfsc catalog (released circa 2000), and 0.037 ± 0.011 counts s^{-1} in the updated rass2rxs (circa 2016). More recently, in 2019 November, Chandra carried out a 9 ks pointing on 31 Aql with the High-Resolution Camera (HRC-I: ObsID 22309; PI: T. Metcalfe). Although HRC-I lacks any meaningful energy resolution, it was the only viable option for the soft coronal source 31 Aql—the other Chandra camera (ACIS) is affected by an ongoing organic contamination issue that severely reduces the sensitivity to low-energy photons. Further, there were no observations of 31 Aql listed in the archives of the other main contemporary high-energy facilities: XMM-Newton and the Swift X-ray Telescope.

Figure 3 is a photon map, in relative sky coordinates, of the center of the HRC-I field, showing a prominent point source within 0″.4 of the predicted location of the bright star in that epoch (typical of the accuracy of the Chandra aspect solution). There are no other significant X-ray point sources in the 50″ × 50″ field. The small red circle indicates the adopted 3″-diameter detection cell (95% encircled energy). The Washington Double Star Catalog reports a faint visual component "E" to 31 Aql (WDS J19250+1157A) in 2002 at a position angle of 288°, separation of 4″.2, and a magnitude deficit of ≈7 in the K band. However, Gaia Data Release 3 (DR3; epoch 2015.5) lists no entries within 30″ of the nearby subgiant brighter than $G = 17$ or with a parallax greater than 1 mas, so component E must have been a background object not sharing the high proper motion of 31 Aql.

The 31 Aql HRC-I level 2 event list from the Chandra Archive was processed as described by T. Ayres (2025). The gross number of counts in the 3″-diameter detection cell was 89 ± 9.4 in the 8.99 ks of dead-time-corrected exposure. The background was sampled in an annulus 50″–60″ from the source, resulting in an areal rate of 3.9×10^{-5} counts (arcsec)$^{-2}$ s^{-1}, typical of HRC-I pointings. This implied a background contribution scaled to the detection cell of 2.5 counts. The net HRC-I count rate, corrected for the encircled energy factor, was 0.0101 ± 0.0011 counts s^{-1}. As shown in Figure 3, there was no obvious variability of the source (e.g., flare activity) when the event list was blocked into multiple time segments (six was the maximum given the low count rate).

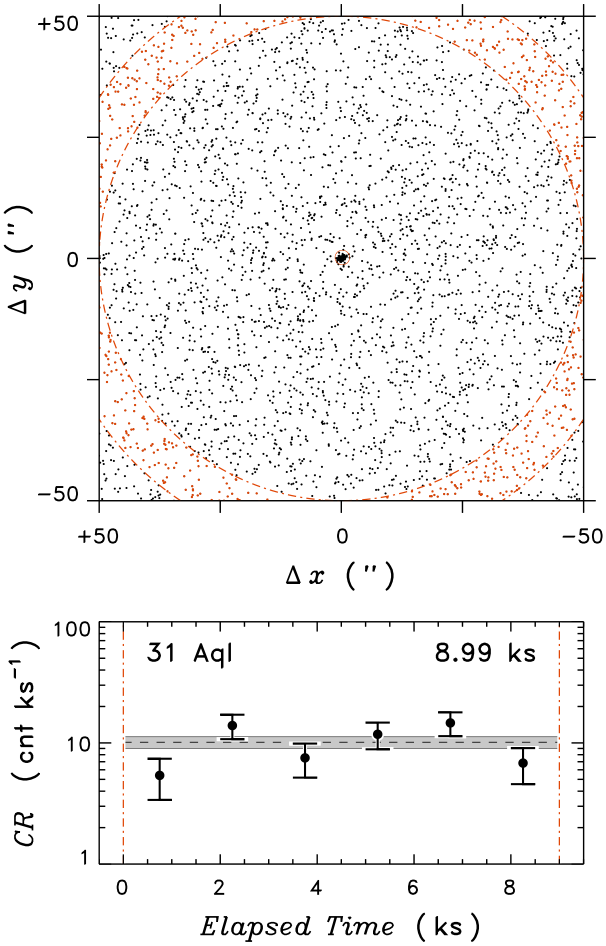

Figure 3. Top: photon map derived from the 2019 Chandra HRC-I pointing on 31 Aql. The axes are sky coordinates relative to the source centroid. The small red circle is the 3″ detection cell; the outer red circles and red dots delimit the background extraction zone. Bottom: time-binned X-ray count rates (Δt = 1500 s) from the HRC-I pointing, corrected for background and the encircled energy fraction, as a function of elapsed time (the dead-time-corrected exposure was 8.99 ks). The gray band indicates the average count rate and $\pm 1\sigma$ Poisson uncertainty for the full observation.

The ROSAT/PSPC and Chandra/HRC-I count rates were then calibrated into flux units by calculating optimum energy conversion factors (ECFs) for the two instrument configurations based on a grid of coronal emission-measure models (see T. Ayres 2025 for details). An apparent slow systematic decline of the HRC-I sensitivity since 2016 was taken into account. The ECF optimization made use of the adopted fundamental parameters of 31 Aql, namely $T_{\rm eff} = 5587$ K and $f_{\rm bol} = 2.24 \times 10^{-7}$ erg s^{-1} cm^{-2}, and a hydrogen column density to the nearby star (d = 14.92 pc) of $N_{\rm H} = 1 \times 10^{18}$ cm^{-2}.

The ROSAT rass2rxs count rate yielded an X-ray luminosity $L_{\rm X} = (4.5 \pm 1.3) \times 10^{27}$ erg s^{-1}, while the Chandra HRC-I result was somewhat lower, $L_{\rm X} = (2.4 \pm 0.3) \times 10^{27}$ erg s^{-1}.

The HRC-I luminosity is consistent with the less certain rass2rxs value, within the typical ranges of short-term and long-term variability seen in normal stars (T. Ayres 2025). We adopt the higher-quality HRC-I X-ray luminosity, recognizing that a factor of 2 uncertainty would not be unusual. However, as noted in Section 2.5, the chromospheric activity level of the star was relatively constant between the epochs of the ROSAT and Chandra pointings.

We can estimate the mass-loss rate of 31 Aql by combining the adopted X-ray luminosity with the stellar radius determined from asteroseismology (see Section 3.1). For stars with mass-loss rates inferred directly from observations of Lyα, there is an empirical relation between the mass-loss rate and the X-ray flux per unit surface area, $\dot{M} \propto F_X^{1.29\pm0.16}$ (B. E. Wood 2018). The resulting estimate is slightly above the solar value, $\dot{M} = 1.05^{+1.08}_{-0.58}\ \dot{M}_\odot$. The uncertainty accounts for the errors on L_X, R, and the power-law exponent combined in quadrature with a factor of 2 systematic uncertainty on the empirical relation (B. E. Wood et al. 2005).

2.4. Hubble Space Telescope Data

As a probe of the physical environment between the photosphere and the corona, we also observed 31 Aql using the Cosmic Origins Spectrograph on the Hubble Space Telescope (HST). The description below closely follows a similar analysis of λ Ser by T. S. Metcalfe et al. (2023b). We obtained a low-resolution G140L far-UV (FUV) spectrum with an integration time of ≈1940 s on 2020 March 2 (program 15991), which was reduced with standard pipeline processing. We computed integrated fluxes for isolated emission lines in the rest frame of the star above nearby pseudo-continua, together with rms errors. We estimated continua from linear fits to clusters of low points on either side of the line in question. When the target line was blended, two methods were employed. Some weaker blends were removed by fitting a Voigt function to better mimic the convolved instrumental profile and line shape, leaving the residual target line for flux integration as before. In some cases, we fit the entire complex of lines with multiple Voigt functions. The results are listed in Table 2. Tests on isolated lines demonstrated that straight integration and Voigt fitting yielded similar results, typically within ±5%. In several cases, multiple nearby lines of the same ion were combined. Following T. R. Ayres (2020), we also measured a 10 Å segment of relatively line-free FUV pseudo-continuum centered at 1506 Å.

We can compare the FUV fluxes of 31 Aql to the Sun (T. R. Ayres 2020) and to λ Ser (T. S. Metcalfe et al. 2023b), a somewhat hotter solar analog (see Table 3). With the exception of the hottest lines, 31 Aql generally shows surface fluxes quite similar to the Sun. The lower chromospheric surface flux in C II (with temperatures of peak emissivity $\log T_{\rm peak} = 3.8$) is 1.3 times smaller than λ Ser; the upper chromospheric C II flux ($\log T_{\rm peak} = 4.5$) is similarly ≈1.5× reduced. In hotter lines formed in the stellar transition region, C III ($\log T_{\rm peak} = 4.8$) is ≈1.9× weaker relative to λ Ser; Si IV ($\log T_{\rm peak} = 4.9$) is similarly reduced. In the C IV doublet ($\log T_{\rm peak} = 5.0$), fluxes are somewhat stronger: a factor of ≈1.7 lower than λ Ser, and 10% weaker than the solar value (here some optical depth effects may play a role).

A number of density-sensitive line ratios can be found in the HST spectra. We use a combination of these results to estimate the electron density in the stellar transition region. The ratio C III(1908 Å)/Si IV(1402 Å), with $\log T_{\rm peak} \sim 4.8$, gives $\log n_e = 9.98^{+0.05}_{-0.06}$. The Si III(1892 Å)/C III(1909 Å) ratio, with $\log T_{\rm peak} \sim 4.7$, yields $\log n_e = 9.87^{+0.08}_{-0.18}$ following F. P. Keenan et al. (1987). The ratios O III(1666 Å)/Si IV (1402 Å) and C III(1908 Å)/O III(1666 Å), also with $\log T_{\rm peak} \sim 4.8$, were less certain, affected by larger errors in the O III line; these yield $\log n_e = 10.80^{+0.40}_{-0.41}$ and $9.76^{+0.30}_{-1.44}$, respectively (following F. P. Keenan et al. 1988). Combining the diagnostics, we find an average $\langle \log n_e \rangle = 9.95 \pm 0.05$ at

Table 2
Measured FUV Line Fluxes for 31 Aql

Ion(s)	Wavelength (Å)	Flux at Earth (10^{-15} erg cm^{-2} s^{-1})
C III[a]	1175	10.1 ± 1.3
O I[a]	1304	55.4 ± 1.1
C II[a]	1335	30.5 ± 0.9
Cl I[b]	1351.7	1.1 ± 0.3
O V	1371	0.21 ± 0.1
Si IV	1393.8	8.0 ± 0.7
O IV	1399.8	0.10 ± 0.3
O IV	1401.2	0.48 ± 0.3
Si IV[b]	1402.8	5.5 ± 0.6
Si IV+O IV[b]	1404.8	0.24 ± 0.6
O IV[b]	1407.4	0.21 ± 0.16
Continuum[c]	1506	3.7 ± 0.8
Si II	1526.5	1.6 ± 0.9
Si II	1533.7	2.4 ± 0.8
C IV[b]	1548	15.3 ± 1.3
C IV[b]	1550	7.7 ± 1.1
C I[a,b]	1561	8.6 ± 1.0
He II	1640.7	6.2 ± 1.5
C I[a]	1657	29.9 ± 2.5
O III	1666.2	1.7 ± 1.2
Si II	1808.0	22.4 ± 3.1
Si II	1817.1	61.6 ± 5
Al III	1854.6	7.1 ± 3.6
Si III	1892.0	20.6 ± 6.6
C III	1908.7	11.8 ± 7.9

Note. All fluxes are from direct integration, except when
[a] multiple lines are combined,
[b] a Voigt function is used for fitting and deblending, or
[c] a ± 5Å integration is performed over a largely line-free region.

Table 3
Comparison of FUV Surface Fluxes

Ion(s)	Wavelength (Å)	Surface Flux (10^3 ergs cm^{-2} s^{-1}) 31 Aql	λ Ser	Sun[b]
C III[a]	1175	2290	4400	2250
O I[a]	1304	12600	8230	5490
C II[a]	1335	6940	10700	7000
Cl I	1351.7	245	330	252
Si IV	1393.8	1830	4110	1690
Si IV	1402.8	1260	1870	875
Continuum	1506	830	3210	1780
C IV	1548	3490	6030	3800
C IV	1550	1760	2730	1960

Notes.
[a] Multiple lines combined.
[b] Results from T. R. Ayres (2020).

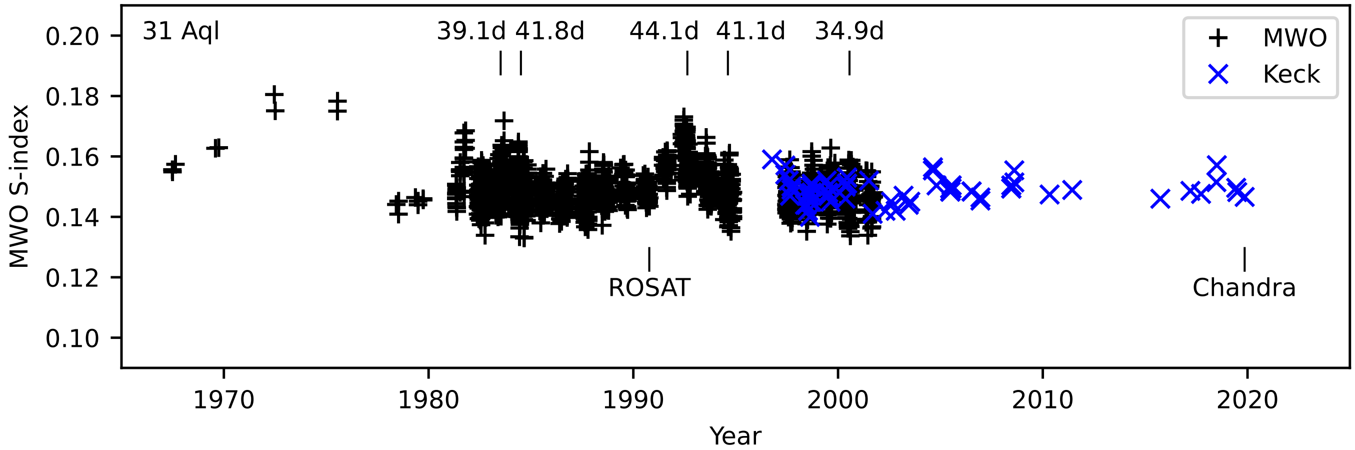

Figure 4. Chromospheric activity measurements of 31 Aql spanning more than 50 yr from Mount Wilson (black plus) and Keck (blue cross), showing minimal long-term variability but sufficient short-term variability to measure the rotation period. Data are from A. C. Baum et al. (2022).

$\log T_{\rm peak} \sim 4.8$. For comparison, $\langle \log n_e \rangle = 10.0$ using the hotter O IV ratio in the Sun (e.g., Y. K. Rao et al. 2022). This suggests that 31 Aql has transition region densities similar to, or perhaps slightly lower than, the Sun at fixed temperature, consistent with its lower surface gravity. We caution, however, that assumptions intrinsic to the line-ratio method make the results uncertain (see discussion in P. G. Judge et al. 2020).

In summary, 31 Aql has chromospheric and transition region fluxes broadly consistent with a star that has similar coronal activity, though slightly lower density, than the Sun. It is also a factor of ~1.3–2 less active than the evolved solar analog λ Ser, with larger reductions toward hotter lines.

2.5. Chromospheric Activity Data

The Mount Wilson Observatory (MWO) HK Project (O. C. Wilson 1978; S. L. Baliunas et al. 1995) defined the *S*-index of chromospheric activity based on the core of the Ca II H & K emission lines relative to nearby pseudo-continuum bands (A. H. Vaughan et al. 1978). A. C. Baum et al. (2022) combined these data with observations from the Keck High Resolution Echelle Spectrometer, and the composite time series is shown in Figure 4. The combined time series shows more than 50 yr of relatively flat activity punctuated by a few periods of enhanced activity. Observations are sparse from 1966 to 1982, as well as during the Keck time series, but the period from 1982 through 2001 has a sufficient number of observations per season to attempt to measure a seasonal rotation period. As described in R. A. Donahue et al. (1996), the range of seasonal rotation periods is presumed to be due to surface features (spots or faculae) transiting the star at different rates due to DR.

Using the methods described in T. S. Metcalfe et al. (2023b), we analyzed 14 out of 24 MWO seasons with $N \geqslant 20$ observations using the Lomb–Scargle periodogram in a Monte Carlo fashion to estimate the seasonal rotation period, false-alarm probability (FAP), and uncertainty in period. We detected significant seasonal rotation periods (FAP < 5%; 95% confidence) in six out of 14 seasons. The results are listed in Table 4, along with the seasonal mean *S*-index. Five of the six significant periods were detected near times of high activity; there are local maxima in the seasonal mean time series in 1983, 1989, 1992, and 1999. This is to be expected, as the *S*-index is enhanced by the presence of magnetic regions on the surface, and larger magnetic regions at activity maximum would produce a stronger rotational modulation of the *S*-index. The significant rotation signals ranged from 34.9 to 44.1 days, with one outlier (FAP = 3.3%) at 15.1 days in the 1985 season. We reject this period based on the expectation of less extreme DR from observations of the Sun and other stellar analyses (R. A. Donahue et al. 1996). Indeed, with our threshold of FAP < 5% we expect a spurious detection in one of 20 seasons, on average, with the FAP defined as the probability of pure noise producing a peak above the selected power threshold. Excluding the 1985 season and taking the error-weighted mean of the remaining seasonal periods, we find a mean rotation period of $P_{\rm rot} = 40.3 \pm 1.5$ days, where the uncertainty is the error in the mean, $\sigma/\sqrt{N}$.

Table 4
Seasonal Measurements from the MWO Data

Season	N	$\langle S \rangle$	$P_{\rm rot}$ (days)	FAP (%)
1983	69	0.1523 ± 0.0050	39.1 ± 0.6	0.0056
1984	75	0.1499 ± 0.0006	41.8 ± 0.4	0.0006
1992	36	0.1599 ± 0.0010	44.1 ± 0.5	0.0556
1994	45	0.1486 ± 0.0006	41.1 ± 3.0	2.3
2000	25	0.1482 ± 0.0012	34.9 ± 0.5	2.6

The range of the seasonal rotation periods $\Delta P = P_{\rm max} - P_{\rm min}$ is 9.2 days. This compares well to the work of R. A. Donahue et al. (1996), who found a power-law relationship $\Delta P \propto P^{1.3\pm0.1}$ for an ensemble of stars in the MWO survey. The authors did not publish the proportionality constant, but using their data for the Sun ($P_{\rm rot} = 26.09$ days, $\Delta P = 4.0$ days), we find it to be $C = 0.0576$. Finally, using $\Delta P_{\rm D96} = CP^{1.3}$ with our mean rotation period, we obtain the empirical range of 7.0 days, comparable to our measured value of 9.2 days (5.0 days if we exclude $P_{\rm rot} = 34.9$ days, which has the largest FAP). This provides additional confidence that we have found a reasonable spread in rotation periods consistent with DR. It likely represents a lower limit on the magnitude of DR, as magnetic features are not expected to appear at all latitudes.

R. A. Donahue (1993) further examined stellar DR by constructing an "active region migration diagram" consisting of seasonal $P_{\rm rot}$ versus mean seasonal activity $\langle S \rangle$. For the Sun, this produces a wedge-like diagram, as the solar cycle begins with low activity and long rotation periods as spots emerge at the highest latitudes, proceeds to high-activity solar maximum with midlatitude spots and medium rotation periods, and finishes with low activity again and fast rotation as spots appear near the equator. The authors proposed that, assuming solar-like active region migration from high to low latitudes (an unsupported assumption), antisolar DR would manifest as a similar wedge-like pattern in opposite time order. R. A. Donahue (1993) identified several candidates for antisolar DR using this technique. We attempted to apply this technique to our data for 31 Aql, but there are not enough sequential seasonal rotation measurements, and the activity does not have sufficiently long rise/decline phases to make the method applicable. Therefore, while we find that 31 Aql has a range of seasonal rotation periods consistent with DR, we cannot determine whether it follows a solar-like or antisolar pattern from the available rotation and activity data alone.

2.6. Spectral Energy Distribution

To obtain a luminosity constraint for asteroseismic modeling, we performed an analysis of the broadband SED of 31 Aql together with the Gaia DR3 parallax (with no systematic offset applied; see, e.g., K. G. Stassun & G. Torres 2021), following the procedures described in K. G. Stassun & G. Torres (2016) and K. G. Stassun et al. (2017, 2018). We obtained JHK_S magnitudes from the Two Micron All Sky Survey, *UBV* magnitudes from the homogeneous photometric catalog of J. C. Mermilliod (2006), and Strömgren *uvby* magnitudes from E. Paunzen (2015). Together, the available photometry spans the full optical–IR stellar SED over the wavelength range 0.3–2 μm.

We performed a fit using Kurucz stellar atmosphere models, with the effective temperature $T_{\rm eff}$, surface gravity $\log g$, and the metallicity [M/H] adopted from J. M. Brewer et al. (2016). The extinction A_V was set to zero based on the proximity of the system. The resulting fit has a reduced $\chi^2 = 1.2$. Integrating the model SED gives the bolometric flux at Earth, $f_{\rm bol} = 2.243 \pm 0.079 \times 10^{-7}$ erg s^{-1} cm^{-2}. Taking the $f_{\rm bol}$ together with the Gaia parallax directly yields the bolometric luminosity, $L_{\rm bol} = 1.557 \pm 0.055\ L_\odot$. The stellar radius follows from the Stefan–Boltzmann relation, giving $R = 1.333 \pm 0.024\ R_\odot$. In addition, we can estimate the stellar mass from the empirical relations of G. Torres et al. (2010), giving $M = 1.14 \pm 0.07\ M_\odot$.

3. Modeling

Below we use the observational constraints from Section 2 to infer additional characteristics of 31 Aql from stellar modeling. In Section 3.1, we determine precise stellar properties from asteroseismic modeling. In Section 3.2, we estimate the wind-braking torque from the prescription of A. J. Finley & S. P. Matt (2018). Finally, in Section 3.3, we constrain the angular momentum history from rotational evolution modeling.

3.1. Asteroseismology

Using the oscillation frequencies identified in Table 1, spectroscopic parameters from J. M. Brewer et al. (2016), and the luminosity constraint from Section 2.6, five teams inferred the properties of 31 Aql from asteroseismic modeling. A variety of stellar evolution codes and fitting methods were used, including ASTEC/AMP 1.3 (J. Christensen-Dalsgaard 2008; T. S. Metcalfe et al. 2009; O. L. Creevey et al. 2017), GARSTEC/BASTA (V. Aguirre Børsen-Koch et al. 2022), MESA/AMP 2.0 (B. Paxton et al. 2015; T. S. Metcalfe et al. 2023a), and YREC (P. Demarque et al. 2008). We found reasonable agreement between the results for the asteroseismic properties, with individual estimates ranging from $R = 1.341$–$1.397\ R_\odot$, $M = 1.02$–$1.15\ M_\odot$, and stellar ages between 8.3 and 10.1 Gyr. We adopt the values and uncertainties from the AMP 2.0 pipeline, which yielded stellar properties most representative of the ensemble of results and produced an optimal reference model with a reduced $\chi^2 \sim 1$. The adopted properties for 31 Aql are summarized in Table 5.

Table 5
Adopted Properties of the Subgiant 31 Aql

	31 Aql	Source
$T_{\rm eff}$ (K)	5587 ± 78	(1)
[M/H] (dex)	+0.32 ± 0.07	(1)
$\log g$ (dex)	4.15 ± 0.08	(1)
$v \sin i$ (km s^{-1})	1.3 ± 0.5	(1)
$B - V$ (mag)	0.77	(2)
$\log R'_{\rm HK}$ (dex)	−5.099	(2)
Inclination (deg)	61	(3)
$\lvert B_{\rm d}\rvert$ (G)	8.5 ± 1.1	(3)
L_X (10^{27} erg s^{-1})	2.4 ± 0.3	(4)
Mass-loss rate ($\dot{M}_\odot$)	$1.05^{+1.08}_{-0.58}$	(4)
$P_{\rm rot}$ (days)	40.3 ± 1.5	(5)
Luminosity ($L_\odot$)	1.557 ± 0.055	(6)
Radius ($R_\odot$)	1.358 ± 0.016	(7)
Mass ($M_\odot$)	1.07 ± 0.04	(7)
Age (Gyr)	8.9 ± 1.3	(7)
Torque (10^{30} erg)	$3.22^{+2.52}_{-1.53}$	(8)
Rossby number (Ro$_\odot$)	1.29 ± 0.06	(9)

References. (1) J. M. Brewer et al. (2016); (2) S. Baliunas et al. (1996); (3) Section 2.2; (4) Section 2.3; (5) Section 2.5; (6) Section 2.6; (7) Section 3.1; (8) Section 3.2; (9) Section 3.3.

The AMP 2.0 pipeline (T. S. Metcalfe et al. 2023a) uses a parallel genetic algorithm (T. S. Metcalfe & P. Charbonneau 2003) to optimize the match between the observational constraints and stellar models produced by version r12778 of the MESA stellar evolution code (B. Paxton et al. 2015) and version 6 of the GYRE pulsation code (R. H. D. Townsend & S. A. Teitler 2013). The stellar models use the default MESA equation of state, primarily from OPAL (F. J. Rogers & A. Nayfonov 2002) and SCVH (D. Saumon et al. 1995), OPAL opacities supplemented with low-temperature values from J. W. Ferguson et al. (2005), the N. Grevesse & A. J. Sauval (1998) solar mixture, NACRE nuclear reaction rates (C. Angulo et al. 1999), a gray atmosphere with A. S. Eddington (1926) T–τ integration, the mixing-length formalism of J. P. Cox & R. T. Giuli (1968), diffusion and settling of helium and heavy elements from A. A. Thoul et al. (1994), and the two-term W. H. Ball & L. Gizon (2014) prescription for the asteroseismic surface correction. The values and uncertainties of the asteroseismic properties were determined from the likelihood-weighted mean and standard deviation of all models sampled by the genetic algorithm during the optimization.

3.2. Magnetic Evolution

We can now estimate the current wind-braking torque for 31 Aql using the prescription of A. J. Finley & S. P. Matt

(2018). Combining the large-scale magnetic field strength derived from spectropolarimetry in Section 2.2, the mass-loss rate inferred from the X-ray surface flux in Section 2.3, the mean rotation period from the chromospheric activity data in Section 2.5, and the precise stellar mass and radius from asteroseismology in Section 3.1, our wind-braking torque estimate is $3.22^{+2.52}_{-1.53} \times 10^{30}$ erg. The dominant contributions to the total torque uncertainty (+78%, −48%) come from the errors on the estimated mass-loss rate (+47%, −35%) and the dipole field strength (±12%), followed by smaller contributions from the rotation period (±4%), the stellar radius (±4%), and the stellar mass (±1%). Similar estimates of the wind-braking torque using the values of $B_{\rm q}$ or $B_{\rm o}$ derived in Section 2.2 yield $3.08^{+2.77}_{-1.58} \times 10^{30}$ erg (quadrupole) or $1.10^{+1.21}_{-0.63} \times 10^{30}$ erg (octupole), consistent with the range of values found from $B_{\rm d}$.

The wind-braking torque for 31 Aql is nearly an order of magnitude stronger than that of the younger solar analog 16 Cyg A (see T. S. Metcalfe et al. 2022). The two stars have nearly the same mass and chromospheric activity, but 31 Aql has a lower surface gravity, larger radius, and slightly higher luminosity than 16 Cyg A, as well as an asteroseismic age that is about 1.5 Gyr older. Despite the difference in metallicity, if we treat these two stars as an evolutionary sequence we can investigate the sources of the large difference in their wind-braking torques by changing one parameter at a time between the fiducial models for each star. We find that the large increase in the wind-braking torque in this age range (7.4–8.9 Gyr) is driven primarily by the much stronger dipole field (+1240%), along with the slightly larger radius (+39%) and higher mass-loss rate (+7%) of 31 Aql, offset by the substantially longer rotation period (−49%).

Considering the simulation results of Q. Noraz et al. (2024), it is possible that 31 Aql may have reached the higher-Ro regime where DR is predicted to shift from solar-like (fast equator, slow poles) to antisolar (slow equator, fast poles). This transition apparently leads to a restoration of the large-scale magnetic field on the subgiant branch, after a prolonged phase of WMB during the second half of the main-sequence lifetime. Unlike the large-scale fields of younger main-sequence stars, the field produced by antisolar DR in the simulations is stationary rather than cycling—in agreement with the flat activity record shown in Figure 4. We hypothesize that the restoration of the large-scale magnetic field with the transition to antisolar DR produces a phase of revived magnetic braking on the subgiant branch. We explore this scenario using a toy model in the following section.

3.3. Rotational Evolution

If we model 31 Aql with assumptions identical to those in T. S. Metcalfe et al. (2025) but including an asteroseismic prior on the stellar age (a Gaussian centered at 8.9 Gyr with $\sigma = 1.3$ Gyr), we predict a rotation period $P_{\rm rot} = 33 \pm 4$ days under WMB and $P_{\rm rot} = 58 \pm 9$ days under a standard spin-down scenario—both in mild tension with the observed rotation period. 31 Aql appears to be a contradiction: It exhibits an observed instantaneous torque consistent with standard braking, yet it could not have undergone that level of spin-down for its lifetime and still retain its relatively rapid rotation. The simulations of Q. Noraz et al. (2024) suggest a possible means to reconcile these observations: The establishment of antisolar DR may eventually restore the torque.

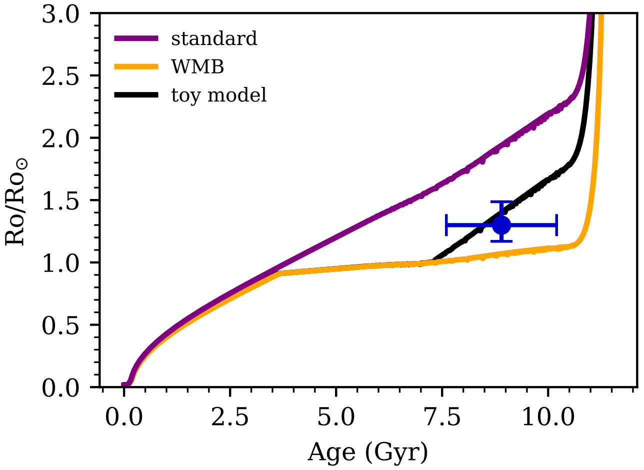

Figure 5. Rossby number as a function of time for a standard spin-down model (purple), WMB model (orange), and a toy model in which braking ceases at $\rm Ro_{crit}$ and resumes at $\rm Ro_{flip}$ (black). The standard and WMB cases are the median posterior tracks for models constrained to match the surface temperature, radius, and metallicity with an informative asteroseismic age prior. The black curve adds the parameter $\rm Ro_{flip}$ by including the observed rotation period as a constraint on the model.

To examine this scenario, we construct a toy model that incorporates a phase of WMB that begins at $\rm Ro_{crit}$, with revived magnetic braking at a higher Ro where DR is thought to flip from solar-like to antisolar ($\rm Ro_{flip}$). The model adopts solid-body rotation, although the DR profile may influence the torque (e.g., A. J. Finley & A. S. Brun 2023; T. Tokuno et al. 2023). In this toy model, both transitions are abrupt: Angular momentum loss is set to zero at $\rm Ro_{crit}$ and restored to the standard braking value after $\rm Ro_{flip}$, based on the instantaneous rotation period and stellar structure. In between these two transitions, the rotational evolution is dictated solely by the evolving moment of inertia as the star gradually expands on the main sequence. Despite the lack of a wind-braking torque, Ro slowly increases with time during this phase (see the orange line in Figure 5).

We fit for a value of $\rm Ro_{flip}$ using the following procedure. We fix the values of $\rm Ro_{crit}$ and the braking normalization (f_k) to those determined in N. Saunders et al. (2024) for WMB, but we leave $\rm Ro_{flip}$ as a free parameter (along with the model mass, metallicity, age, and mixing length). The prior on $\rm Ro_{flip}$ is uninformative aside from two limits: $\rm Ro_{flip} > Ro_{crit}$ and the stellar age at $\rm Ro_{flip}$ must be less than the current age. This effectively incorporates a prior informed by the observed wind-braking torque for 31 Aql.

We include the rotation period as a constraint on the model, adopting the value from Section 2.5 with an additional 10% error on the period added in quadrature, to account for systematic uncertainty in the observed active latitudes (e.g., C. R. Epstein & M. H. Pinsonneault 2014). As in T. S. Metcalfe et al. (2025), the observed $T_{\rm eff}$, [M/H], and radius are used as constraints on the model, with values and errors adopted from Table 5, along with additional systematic uncertainties added in quadrature.

We find $\rm Ro_{flip} = 1.1 \pm 0.05\ Ro_{crit}$. Because the evolution between $\rm Ro_{crit}$ and $\rm Ro_{flip}$ is driven by slow structural changes to the star over a nuclear timescale, there is a sizable delay before the star reaches $\rm Ro_{flip}$—in our model for 31 Aql, braking resumes $3.5^{+1.3}_{-2.2}$ Gyr after the onset of WMB, at an age of $7.1^{+1.6}_{-2.5}$ Gyr. This represents a substantial fraction of the

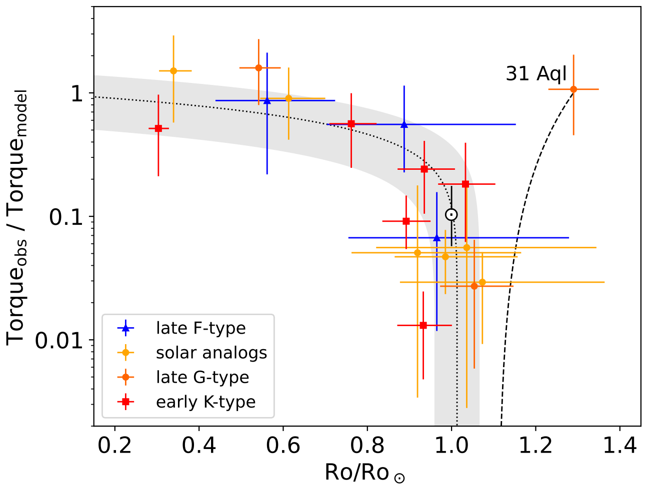

Figure 6. Ratio of the observationally estimated and model wind-braking torque as a function of the Rossby number normalized to the solar value. The dotted line and gray shaded region illustrate the fit and 95% confidence interval described by T. S. Metcalfe et al. (2025). The revived magnetic braking in 31 Aql at higher Ro is evident, and quadratic growth is illustrated schematically with a dashed line.

main-sequence lifetime. The long pause in spin-down means that our toy model preserves many of the broad features of the original WMB model: Stars undergo a prolonged phase of subdued spin-down during the latter half of the main sequence, and thus a sizable population of objects should be observed in the midst of WMB.

4. Discussion

The estimated wind-braking torque and current Ro of 31 Aql appear to constrain the transition from solar-like to antisolar DR in subgiant stars. In Figure 6, we reproduce the evidence from T. S. Metcalfe et al. (2025) for the gradual onset of WMB in older main-sequence stars, to which we add the new constraint from the G7 subgiant 31 Aql (labeled orange point). The efficiency of magnetic braking decreases by up to 2 orders of magnitude as stars approach $\mathrm{Ro}_{\mathrm{crit}}$, slightly above the solar value. To explain the current wind-braking torque and rotation period of 31 Aql, we find that standard magnetic braking may resume near 1.1 $\mathrm{Ro}_{\mathrm{crit}}$, apparently due to a restoration of the large-scale magnetic field associated with a shift in the DR pattern from solar-like to antisolar, as suggested by recent simulations (Q. Noraz et al. 2024).

Although we cannot directly constrain the sense of the DR from the chromospheric activity data, the observations reveal a variety of rotation periods in different seasons and minimal long-term variability on cycle timescales, consistent with the simulations. Previous support for the simulation results came from observations of enhanced photometric variability in Kepler targets at Ro above the solar value (S. Mathur et al. 2025), but 31 Aql suggests that the transition to antisolar DR might be accompanied by a restoration of the large-scale magnetic field and revived magnetic braking.

The revived magnetic braking due to antisolar DR is distinct from the born-again dynamo phenomenon discovered in 94 Aqr Aa (T. S. Metcalfe et al. 2020) and confirmed in β Hyi (T. S. Metcalfe et al. 2024; A. R. G. Santos et al. 2025). The latter occurs in stars with shallower convective envelopes, when physical expansion on the subgiant branch initially pushes the Ro above $\mathrm{Ro}_{\mathrm{crit}}$, which is thought to lead to a shutdown of the cycling global dynamo. However, subsequent structural evolution pushes the Ro back below $\mathrm{Ro}_{\mathrm{crit}}$, apparently reinvigorating the dynamo near the base of the red giant branch. Stars with deeper convection zones like 31 Aql do not experience a "blue hook" in the Hertzsprung–Russell diagram, but instead stellar evolution models show a steadily increasing Ro along the subgiant branch. This steady evolution apparently leads to a shutdown of the cycling global dynamo when Ro exceeds $\mathrm{Ro}_{\mathrm{crit}}$, followed by revived magnetic braking when Ro exceeds $\mathrm{Ro}_{\mathrm{flip}}$, together with the emergence of a noncycling large-scale magnetic field. Despite these distinct trajectories, it is possible that stars with born-again dynamos might have exceeded $\mathrm{Ro}_{\mathrm{flip}}$ somewhere along their evolutionary paths, potentially providing complementary constraints on $\mathrm{Ro}_{\mathrm{flip}}$.

A more sophisticated treatment of the rotational evolution would incorporate the gradual onset of WMB as Ro approaches $\mathrm{Ro}_{\mathrm{crit}}$, and the gradual resumption of magnetic braking above $\mathrm{Ro}_{\mathrm{flip}}$. In contrast, our toy model incorporates step functions, eliminating magnetic braking at $\mathrm{Ro}_{\mathrm{crit}}$ and restoring it at $\mathrm{Ro}_{\mathrm{flip}}$. The functional form of the gradual onset shown in Figure 6 is a generic prediction of a Hopf bifurcation, with the dynamo efficiency decreasing as $\sqrt{\mathrm{Ro}_{\mathrm{crit}} - \mathrm{Ro}}$ (R. H. Cameron & M. Schüssler 2017). This treatment is appropriate for the transition from an oscillatory to a stationary solution, while the shift from solar-like to antisolar DR in a nonoscillatory dynamo can be described by a transcritical bifurcation with a quadratic growth in dynamo efficiency at $\mathrm{Ro} > \mathrm{Ro}_{\mathrm{flip}}$ (dashed line in Figure 6). A refined analysis that replaces the step functions in our toy model with the expected functional forms for these two transitions could improve our estimate of the absolute value of Ro (not just relative to $\mathrm{Ro}_{\mathrm{crit}}$) at which DR shifts from solar-like to antisolar.

It is important to note that there are still significant uncertainties, both in the observations and the simulations, about the exact timing of the transition from solar-like to antisolar DR. The value of $\mathrm{Ro}_{\mathrm{crit}} \sim 1.01\ \mathrm{Ro}_\odot$ found by T. S. Metcalfe et al. (2025) approximately separates stars with cycles at lower Ro and stars with flat activity at higher Ro. This suggests that Ro can exceed $\mathrm{Ro}_{\mathrm{crit}}$ slightly during the latter half of the main-sequence lifetime, due to mild physical expansion even when magnetic braking is substantially weakened. This expansion accelerates during the subgiant phase, and our fit to 31 Aql suggests a value of $\mathrm{Ro}_{\mathrm{flip}} \sim 1.1\ \mathrm{Ro}_{\mathrm{crit}}$, significantly higher than values typically reached on the main sequence. However, with only one star currently available to establish this constraint, the transition to antisolar DR may be possible at lower values of Ro.

The simulations described by A. S. Brun et al. (2022) and analyzed by Q. Noraz et al. (2024) were not designed to probe evolution beyond the main sequence, so their constraints on $\mathrm{Ro}_{\mathrm{flip}}$ may not be entirely correct for a subgiant. Although the authors noted the expected influence of WMB, the simulations attempted to follow the evolution of main-sequence stars under a scenario of standard magnetic braking. As such, the background stellar structure in the simulations at Ro above the solar value was appropriate for evolved main-sequence stars rather than subgiants (see also H. Hotta & Y. Hatta 2026). The limited sampling of Ro in these computationally expensive simulations currently suggests that $\mathrm{Ro}_{\mathrm{flip}}$ lies somewhere between 0.76 and 1.38 $\mathrm{Ro}_\odot$ (see Figure 1 in Q. Noraz et al. 2024). Future simulations in this range of Ro with a background stellar structure appropriate for subgiant stars may provide stronger constraints on the value of $\mathrm{Ro_{flip}}$.

The inclination of 31 Aql ($i \sim 61^\circ$) is favorable for the asteroseismic detection of rotational splittings that could distinguish between solar-like and antisolar DR. In particular, the visibility of both the inner ($m = \pm1$) and outer ($m = \pm2$) components of an $\ell = 2$ quintuplet is optimal at $i = 60^\circ$ (L. Gizon & S. K. Solanki 2003). The latter components ($\ell = m$) probe the equatorial rotation rate, while the former ($\ell \neq m$) probe the rotation at higher latitudes (M. N. Lund et al. 2014), so the relative splittings can reveal the sense of the DR. This technique has already been demonstrated for several dozen Kepler targets (O. Benomar et al. 2018; M. Bazot et al. 2019), though it requires long-term, high-S/N observations. Such measurements may be possible from a careful analysis of KIC 8349582 (Kepler-95), a close analog of 31 Aql in the Kepler field of view. The duration of TESS observations is currently too limited to resolve rotational splittings, and the proposed PLATO fields do not include 31 Aql (V. Nascimbeni et al. 2022). However, the higher S/N achievable with ground-based radial-velocity asteroseismology should be able to resolve the rotational splittings and decipher between solar-like and antisolar DR in 31 Aql. Future multimonth monitoring by the Stellar Observations Network Group (F. Grundahl et al. 2008) may provide the necessary S/N for such measurements.

Acknowledgments

T.S.M. acknowledges support from Chandra award GO0-21005X, NSF grant AST-2205919, TESS General Investigator grant 80NSSC25K7898, and NASA grant 80NSSC25K7563. Computational time at the Texas Advanced Computing Center was provided through ACCESS allocations TG-AST090107 and TG-PHY250037. J.v.S. acknowledges support from NSF grant AST-2205888. D.B. acknowledges support from TESS General Investigator grant 80NSSC19K0385. R.A.G. acknowledges support from a GOLF and PLATO Centre National D'Études Spatiales (CNES) grant. O.K. acknowledges support from the Swedish Research Council (grant agreement No. 2023-03667) and the Swedish National Space Agency. S.H.S. is grateful for support from award HST-GO-15991.002-A. A.S. acknowledges support from the European Research Council (ERC) under the European Union's Horizon 2020 research and innovation program (CartographY; grant agreement 804752). T.R.B. is supported by the Australian Research Council (grant No. FL220100117). S.N.B. acknowledges support from PLATO ASI-INAF agreement No. 2022-28-HH.0, "PLATO Fase D". The TESS and HST data used in this paper can be found on MAST (doi:10.17909/0vak-d288).

ORCID iDs

Travis S. Metcalfe https://orcid.org/0000-0003-4034-0416
Jennifer L. van Saders https://orcid.org/0000-0002-4284-8638
Thomas R. Ayres https://orcid.org/0000-0002-1242-5124
Derek Buzasi https://orcid.org/0000-0002-1988-143X
Jeremy J. Drake https://orcid.org/0000-0002-0210-2276
Ricky Egeland https://orcid.org/0000-0002-4996-0753
Rafael A. García https://orcid.org/0000-0002-8854-3776
Oleg Kochukhov https://orcid.org/0000-0003-3061-4591
Steven H. Saar https://orcid.org/0000-0001-7032-8480
Keivan G. Stassun https://orcid.org/0000-0002-3481-9052
Sarbani Basu https://orcid.org/0000-0002-6163-3472
J. M. Joel Ong https://orcid.org/0000-0001-7664-648X
Amalie Stokholm https://orcid.org/0000-0002-5496-365X
Timothy R. Bedding https://orcid.org/0000-0001-5222-4661
Sylvain N. Breton https://orcid.org/0000-0003-0377-0740
Ilya V. Ilyin https://orcid.org/0000-0002-0551-046X
Pascal Petit https://orcid.org/0000-0001-7624-9222
Marc H. Pinsonneault https://orcid.org/0000-0002-7549-7766
Klaus G. Strassmeier https://orcid.org/0000-0002-6192-6494

References

Aguirre Børsen-Koch, V., Rørsted, J. L., Justesen, A. B., et al. 2022, MNRAS, 509, 4344
Angulo, C., Arnould, M., Rayet, M., et al. 1999, NuPhA, 656, 3
Ayres, T. 2025, AJ, 169, 281
Ayres, T. R. 2020, ApJS, 250, 16
Baliunas, S., Sokoloff, D., & Soon, W. 1996, ApJL, 457, L99
Baliunas, S. L., Donahue, R. A., Soon, W. H., et al. 1995, ApJ, 438, 269
Ball, W. H., & Gizon, L. 2014, A&A, 568, A123
Baum, A. C., Wright, J. T., Luhn, J. K., & Isaacson, H. 2022, AJ, 163, 183
Bazot, M., Benomar, O., Christensen-Dalsgaard, J., et al. 2019, A&A, 623, A125
Benomar, O., Bazot, M., Nielsen, M. B., et al. 2018, Sci, 361, 1231
Bowler, B. P., Tran, Q. H., Zhang, Z., et al. 2023, AJ, 165, 164
Brandenburg, A., & Giampapa, M. S. 2018, ApJL, 855, L22
Breton, S. N., García, R. A., Ballot, J., Delsanti, V., & Salabert, D. 2022, A&A, 663, A118
Brewer, J. M., Fischer, D. A., Valenti, J. A., & Piskunov, N. 2016, ApJS, 225, 32
Brun, A. S., Strugarek, A., Noraz, Q., et al. 2022, ApJ, 926, 21
Cameron, R. H., & Schüssler, M. 2017, ApJ, 843, 111
Christensen-Dalsgaard, J. 2008, Ap&SS, 316, 13
Cox, J. P., & Giuli, R. T. 1968, Principles of Stellar Structure (Gordon and Breach)
Creevey, O. L., Metcalfe, T. S., Schultheis, M., et al. 2017, A&A, 601, A67
Davies, G. R., Silva Aguirre, V., Bedding, T. R., et al. 2016, MNRAS, 456, 2183
Demarque, P., Guenther, D. B., Li, L. H., Mazumdar, A., & Straka, C. W. 2008, Ap&SS, 316, 31
Donahue, R. A. 1993, PhD thesis, New Mexico State Univ.
Donahue, R. A., Saar, S. H., & Baliunas, S. L. 1996, ApJ, 466, 384
Donati, J. F., Semel, M., Carter, B. D., Rees, D. E., & Collier Cameron, A. 1997, MNRAS, 291, 658
Eddington, A. S. 1926, The Internal Constitution of the Stars (Cambridge Univ. Press)
Epstein, C. R., & Pinsonneault, M. H. 2014, ApJ, 780, 159
Ferguson, J. W., Alexander, D. R., Allard, F., et al. 2005, ApJ, 623, 585
Finley, A. J., & Brun, A. S. 2023, A&A, 674, A42
Finley, A. J., & Matt, S. P. 2018, ApJ, 854, 78
Fletcher, S. T., Chaplin, W. J., Elsworth, Y., & New, R. 2008, AN, 329, 447
Foreman-Mackey, D., Hogg, D. W., Lang, D., & Goodman, J. 2013, PASP, 125, 306
García, R. A., Mathur, S., Pires, S., et al. 2014, A&A, 568, A10
Gastine, T., Yadav, R. K., Morin, J., Reiners, A., & Wicht, J. 2014, MNRAS, 438, L76
Gizon, L., & Solanki, S. K. 2003, ApJ, 589, 1009
Grevesse, N., & Sauval, A. J. 1998, SSRv, 85, 161
Grundahl, F., Christensen-Dalsgaard, J., Arentoft, T., et al. 2008, CoAst, 157, 273
Hotta, H., & Hatta, Y. 2026, NatAs, in press
Huber, D., White, T. R., Metcalfe, T. S., et al. 2022, AJ, 163, 79
Jenkins, J. M., Twicken, J. D., McCauliff, S., et al. 2016, SPIE, 9913, 99133E
Judge, P. G., Kleint, L., Leenaarts, J., Sukhorukov, A. V., & Vial, J.-C. 2020, ApJ, 901, 32
Karak, B. B., Käpylä, P. J., Käpylä, M. J., et al. 2015, A&A, 576, A26
Keenan, F. P., Dufton, P. L., Aggarwal, K. M., & Kingston, A. E. 1988, ApJ, 324, 1068
Keenan, F. P., Kingston, A. E., & Dufton, P. L. 1987, MNRAS, 225, 859

Kochukhov, O., Makaganiuk, V., & Piskunov, N. 2010, A&A, 524, A5
Lund, M. N., Chontos, A., Grundahl, F., et al. 2025, A&A, 701, A285
Lund, M. N., Miesch, M. S., & Christensen-Dalsgaard, J. 2014, ApJ, 790, 121
Lund, M. N., Silva Aguirre, V., Davies, G. R., et al. 2017, ApJ, 835, 172
Mathur, S., Santos, Â. R. G., Claytor, Z. R., et al. 2025, ApJ, 982, 114
Mermilliod, J. C. 2006, yCat, II/168
Metcalfe, T. S., Buzasi, D., Huber, D., et al. 2023b, AJ, 166, 167
Metcalfe, T. S., & Charbonneau, P. 2003, JCoPh, 185, 176
Metcalfe, T. S., Creevey, O. L., & Christensen-Dalsgaard, J. 2009, ApJ, 699, 373
Metcalfe, T. S., Egeland, R., & van Saders, J. 2016, ApJL, 826, L2
Metcalfe, T. S., Finley, A. J., Kochukhov, O., et al. 2022, ApJL, 933, L17
Metcalfe, T. S., Kochukhov, O., Ilyin, I. V., et al. 2019, ApJL, 887, L38
Metcalfe, T. S., Townsend, R. H. D., & Ball, W. H. 2023a, RNAAS, 7, 164
Metcalfe, T. S., & van Saders, J. 2017, SoPh, 292, 126
Metcalfe, T. S., van Saders, J. L., Basu, S., et al. 2020, ApJ, 900, 154
Metcalfe, T. S., van Saders, J. L., Huber, D., et al. 2024, ApJ, 974, 31
Metcalfe, T. S., van Saders, J. L., Pinsonneault, M. H., et al. 2025, ApJL, 991, L17
Nascimbeni, V., Piotto, G., Börner, A., et al. 2022, A&A, 658, A31
Nielsen, M. B., Ball, W. H., Standing, M. R., et al. 2020, A&A, 641, A25
Noraz, Q., Brun, A. S., & Strugarek, A. 2024, A&A, 684, A156
Paunzen, E. 2015, A&A, 580, A23
Paxton, B., Marchant, P., Schwab, J., et al. 2015, ApJS, 220, 15
Petit, P., Louge, T., Théado, S., et al. 2014, PASP, 126, 469
Pires, S., Mathur, S., García, R. A., et al. 2015, A&A, 574, A18
Proudman, J. 1916, RSPSA, 92, 408
Rao, Y. K., Del Zanna, G., Mason, H. E., & Dufresne, R. 2022, MNRAS, 517, 1422
Ricker, G. R., Winn, J. N., Vanderspek, R., et al. 2014, SPIE, 9143, 914320
Roca Cortés, T., Jiménez, A., Pallé, P. L. & GOLF TeamVIRGO Team 1999, ESASP, 448, 135
Rogers, F. J., & Nayfonov, A. 2002, ApJ, 576, 1064
Ryabchikova, T., Piskunov, N., Kurucz, R. L., et al. 2015, PhyS, 90, 054005
Santos, A. R. G., Metcalfe, T. S., Kochukhov, O., et al. 2025, A&A, 698, L23
Saumon, D., Chabrier, G., & van Horn, H. M. 1995, ApJS, 99, 713
Saunders, N., van Saders, J. L., Lyttle, A. J., et al. 2024, ApJ, 962, 138
Skumanich, A. 1972, ApJ, 171, 565
Stassun, K. G., Collins, K. A., & Gaudi, B. S. 2017, AJ, 153, 136
Stassun, K. G., Corsaro, E., Pepper, J. A., & Gaudi, B. S. 2018, AJ, 155, 22
Stassun, K. G., & Torres, G. 2016, ApJL, 831, L6
Stassun, K. G., & Torres, G. 2021, ApJL, 907, L33
Strassmeier, K. G., Ilyin, I., Järvinen, A., et al. 2015, AN, 336, 324
Strugarek, A., Beaudoin, P., Charbonneau, P., Brun, A. S., & do Nascimento, J.-D. 2017, Sci, 357, 185
Taylor, G. I. 1917, RSPSA, 93, 99
Thompson, M. J., Toomre, J., Anderson, E. R., et al. 1996, Sci, 272, 1300
Thoul, A. A., Bahcall, J. N., & Loeb, A. 1994, ApJ, 421, 828
Tokuno, T., Suzuki, T. K., & Shoda, M. 2023, MNRAS, 520, 418
Torres, G., Andersen, J., & Giménez, A. 2010, A&ARv, 18, 67
Townsend, R. H. D., & Teitler, S. A. 2013, MNRAS, 435, 3406
van Saders, J. L., Ceillier, T., Metcalfe, T. S., et al. 2016, Natur, 529, 181
Vaughan, A. H., Preston, G. W., & Wilson, O. C. 1978, PASP, 90, 267
Weber, M., Strassmeier, K. G., & Washuettl, A. 2005, AN, 326, 287
Wilson, O. C. 1978, ApJ, 226, 379
Wood, B. E. 2018, JPhCS, 1100, 012028
Wood, B. E., Müller, H. R., Zank, G. P., Linsky, J. L., & Redfield, S. 2005, ApJL, 628, L143